Computer Methods in Applied Mechanics and Engineering 445 (2025) 118200

Contents lists available at ScienceDirect

Comput. Methods Appl. Mech. Engrg.

journal homepage: www.elsevier.com/locate/cma

Solving adhesive rough contact problems with Atomic Force Microscope data

M.R. Marulli [a], J. Bonari [b,a], P. Pingue [c], M. Paggi [a,*]

[a] IMT School for Advanced Studies Lucca, Piazza San Francesco 19, 55100 Lucca, Italy
[b] Institute for the Protection of Terrestrial Infrastructures, German Aerospace Center (DLR), Rathausallee 12, 53757, Sankt Augustin, Germany
[c] NEST - National Enterprise for nanoScience and nanoTechnology, Scuola Normale Superiore and Istituto Nanoscienze - CNR, Piazza San Silvestro 12, 56127 Pisa, Italy

GRAPHICAL ABSTRACT

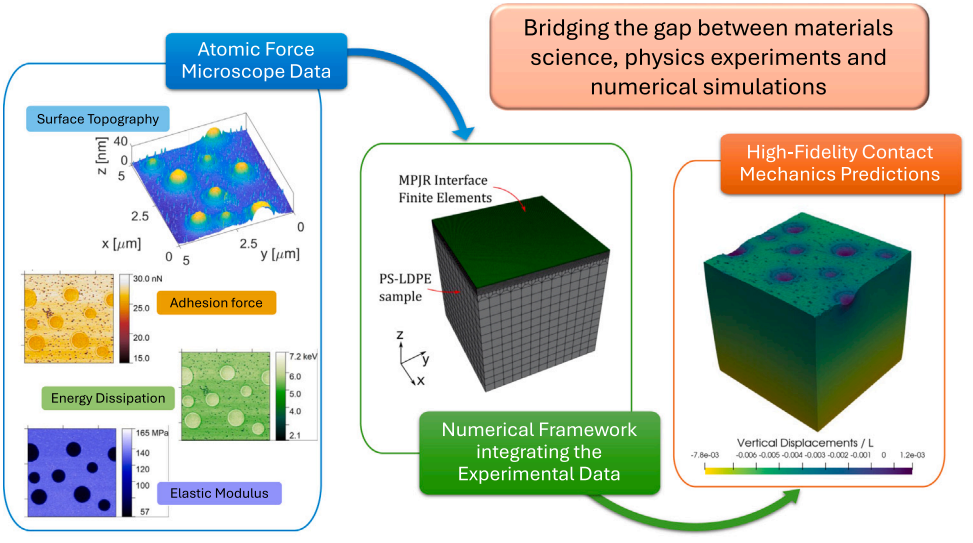

ARTICLE INFO

Keywords:
Contact mechanics
Roughness
Adhesion
MPJR interface finite elements
AFM data integration

ABSTRACT

This study presents an advanced numerical framework that integrates experimentally acquired Atomic Force Microscope (AFM) data into high-fidelity simulations for adhesive rough contact problems, bridging the gap between experimental physics and computational mechanics. The proposed approach extends the eMbedded Profile for Joint Roughness (MPJR) interface finite element method to incorporate both surface topography and spatially varying adhesion properties, imported directly from AFM measurements. The adhesion behavior is modeled

* Corresponding author.
E-mail address: marco.paggi@imtlucca.it (M. Paggi).

https://doi.org/10.1016/j.cma.2025.118200
Received 20 March 2025; Received in revised form 11 June 2025; Accepted 29 June 2025
Available online 17 July 2025

using a modified Lennard-Jones potential, which is locally parameterized based on the AFM-extracted adhesion peak force and energy dissipation data. The effectiveness of this method is demonstrated through 2D and 3D finite element simulations of a heterogeneous PS-LDPE (polystyrene matrix with low-density polyethylene inclusions) sample, where the bulk elastic properties are also experimentally characterized via AFM. The results highlight the significance of accounting for both surface adhesion variability and material bulk heterogeneity in accurately predicting contact responses.

1. Introduction

Contact problems between bodies are a fundamental topic in theoretical and applied mechanics and physics, with several critical applications for tribology in many engineering fields [1,2]. Surface-surface interactions play a key role in stress transfer, friction, wear, heat, and electric conduction. Miniaturization observed nowadays in technology requires the development of high-fidelity contact mechanics simulations accounting for surface textures and microscopic roughness, which are observable over multiple length scales [3].

Adhesion plays a crucial role in micro-scale and nano-scale contact problems, where adhesive tractions influence contact mechanics to varying degrees [4,5]. Adhesion becomes particularly important in micro- and nano-scale contacts, low-load conditions, and soft materials. Thus, adhesive tractions are of great interest especially for the design of nano-devices, bio-systems, thin films, coatings, and layered structures, and affect the performance and durability of components in many engineering applications [6–10]. Moreover, many real-world materials are heterogeneous, introducing further complexities in the contact response. Inhomogeneities can be the source of stress concentrations, leading to fatigue crack nucleation and reduced fatigue strength. However, today, their impact on the adhesive contact of rough surfaces remains challenging to be predicted using numerical methods, often requiring simplified assumptions on the surface roughness and/or the adhesive behavior [11–15].

In this context, numerical solution methods based on the Boundary Element Method (BEM) have seen considerable development [16–20] since they benefit from the sole discretization of the boundary and not of the bulk. To overcome the limitations of this approach, which was originally conceived to deal with linear elastic problems where the Green functions –relating the displacements of the points belonging to the boundary to the applied contact tractions– are known and the principle of superposition can be invoked, significant efforts have been made. In this regard, polarization stress approaches that are used in FFT-based homogenization [21,22] have been applied to generalize volume-based Green's functions methods to solve contact mechanics problems [23] with nonlinear interface and bulk constitutive relations [24–29], thermo-elastic coupled problems [30,31], and also problems with arbitrary heterogeneous inclusions [32–34]. In the method, polarization stress approaches allow treating all the nonlinear and heterogeneous terms as eigen-stress contributions to a linear problem, again allowing the use of Green's functions. However, the convergence of fully coupled (monolithic) treatments of multi-field problems is still an open issue in such methods. Applications of BEM to adhesive contact problems [35–38] and viscoelasticity [39,40] have recently been put forward. Another possible solution strategy consists of semi-analytical solutions as in [24], where they analyzed adhesive contact behavior in heterogeneous elastic materials with engineered rough surfaces. The proposed equivalent inclusion method (EIM), however, assumes idealized inhomogeneities, which may not fully capture complex material structures with graded or anisotropic properties, and the rough surfaces are modeled based on the statistical description of the height field distributions.

To overcome the above limitations in a setting suitable for the treatment of nonlinear coupled problems, the Finite Element Method (FEM) would be the natural remedy. However, due to the higher computational cost associated with the discretization of the bulk and the complexity in meshing nonplanar interfaces, its application to contact problems with roughness has been primarily confined to a few instances [41–48]. Moreover, the convergence of contact search algorithms in multi-scale roughness can be problematic.

To address the challenges outlined above, a finite element discretization technique relying on the eMbedded Profile for Joint Roughness (MPJR) interface finite element, and the associated contact solution scheme, have been firstly proposed in [49] and extended in [50–52] to frictional problems. This novel framework has been developed to solve high-fidelity contact mechanics simulations accounting for surface textures and microscopic roughness. An interface characterized by any arbitrarily complex shape can be globally discretized as smooth. At the same time, any deviation from planarity is embedded into the MPJR interface finite elements to be used as a correction of the normal gap function computed if the surfaces were flat. It applies to both rigid-deformable and deformable-deformable solids in contact and is particularly efficient from the computational point of view for the following principal reasons: (*i*) the interface is globally discretized as nominally flat; (*ii*) any height field perturbing the planarity can be incorporated, either given by a continuous analytical function when available or directly provided by discrete profilometric data; (*iii*) no smoothing or regularization of the height field is required; (*iv*) contact search algorithms can be fully avoided by considering fixed pairing of nodes at the interface.

Moreover, the methodology can be extended to other nonlinear phenomena or multi-field problems. It has been applied to frictional contacts in partial slip [51] and full sliding regime [50] for viscoelastic solids. Moreover, the method has been extended to 3D, including friction and adhesion [52], demonstrating its efficiency through specific benchmark tests on spherical indenters, wavy profiles, fractal surfaces, and cyclic loading, comparing predictions with theoretical solutions and benchmark BEM results. The solution of contact-induced fracture phenomena has been treated in [53], where the MPJR method combined with the phase

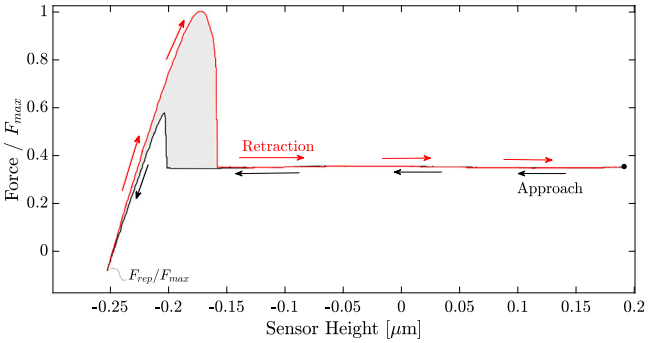

Fig. 1. Experimental force-AFM sensor's position curve measured by the AFM during a cycle of approach-retraction of the tip (having a nominal radius of 25 nm) on the sample. $F_{\max}$ is the peak adhesive force, F_{rep} is the maximum value of the repulsive force, and the shaded area indicates the energy dissipated during the operation.

field approach to brittle fracture for the substrate has been established for the simulation of smooth and rough spherical indentation tests, with a very good agreement with available experimental trends.

The present study extends and exploits the above methodology to solve complex contact problems involving not only experimentally acquired surface topography but also the material heterogeneity and the spatial variation of the adhesive field on the substrate surface. The MPJR framework is therefore extended to consider, in addition to the surface roughness, multiple field variables at the interface level, in particular, collected with an Atomic Force Microscope (AFM).

AFMs are primarily used to obtain topographic information on solid surfaces at the nanometer scale and below. A sharp tip mounted on a cantilever touches the surface, which causes the cantilever to deflect. This deflection is proportional to the forces acting between the microscope tip and the investigated surface [54]. The tip is moved towards the sample until comes in contact with it, and then it is retracted again, while the interaction between the tip and the sample is recorded in a force-AFM sensor's displacement curve (see the experimental curve shown in Fig. 1). This operation is repeated for each surface point to build a map of the tip–surface interaction, and the collected experimental curves are converted to a force versus separation plot for fitting and further analysis. Different surface properties, such as morphology, adhesive force, elastic modulus, and surface deformation, can simultaneously be derived from the force–separation curve. Note that here and in the remainder of the manuscript, positive force values are associated with attractive interactions between the tip and the sample (adhesion); in contrast, repulsive forces have a negative sign, contrary to what is generally assumed for AFM curves.

For the modeling approach presented in this work, the most important quantities that can be derived from the AFM curve are the sample height field, the adhesion force (which is the maximum force reached during the retraction curve denoted by $F_{\max}$), the energy dissipated during the approach-retraction cycle, represented by the shaded area in Fig. 1, and the elastic modulus. The elastic modulus is determined by fitting a portion of the force-distance curves during the retraction phase with a Derjaguin–Muller–Toporov (DMT) model [54,55]. This model approximates the AFM tip as a sphere pressing into a flat surface and links the contact force and the surface deformation to the material modulus, allowing the computation of the value of the substrate elastic modulus once the AFM tip radius and its elastic modulus are known.

The present work describes how the punctual values of adhesion peak force and energy dissipation collected with the AFM can be fully integrated into finite element analyses by their embedding in the MPJR interface finite elements, paving the way to high-fidelity contact mechanics predictions and bridging the gap between materials science, physics experiments, and numerical simulations. The numerical framework is presented in Section 2 and applied to a 3D contact problem in Section 3. The AFM also provides information related to the elastic modulus of the analyzed material. This feature is not directly included in the MPJR finite element since it is a bulk property, but the effect of the material heterogeneity on the contact solution is discussed in Section 4. Specifically, for that special type of heterogeneity stemming from the two polymeric phase materials being considered, the difference in contact predictions in the case of a fully heterogeneous continuum model or a homogenized bulk model is investigated.

2. Numerical framework

The derivation of the MPJR interface finite elements is briefly summarized in this section (the interested reader can refer to [49,52] for more details), focusing on how not only the experimental height field but also the adhesion and dissipation fields have been exploited to formulate the interface constitutive model, allowing for an accurate solution of the contact problem.

Let the contact problem be described by two domains $\Omega_{i=1,2}$ separated by an interface Γ^* with opposite boundaries $\Gamma^*_{i=1,2}$ nominally smooth but microscopically embedding the rough surfaces $\Gamma_{i=1,2}$, as represented in Fig. 2, and by the kinematic quantities governing the contact problem.

In general, two indenting rough surfaces can be modeled in the proposed numerical framework by considering their *composite topography*, see [49]. In this work, for simplicity, the case of a smooth surface in contact with a rough surface Γ is considered. The elevation of Γ is described by a function $h(\xi,\eta)$ where ξ and η are a set of curvilinear coordinates defining a point-wise

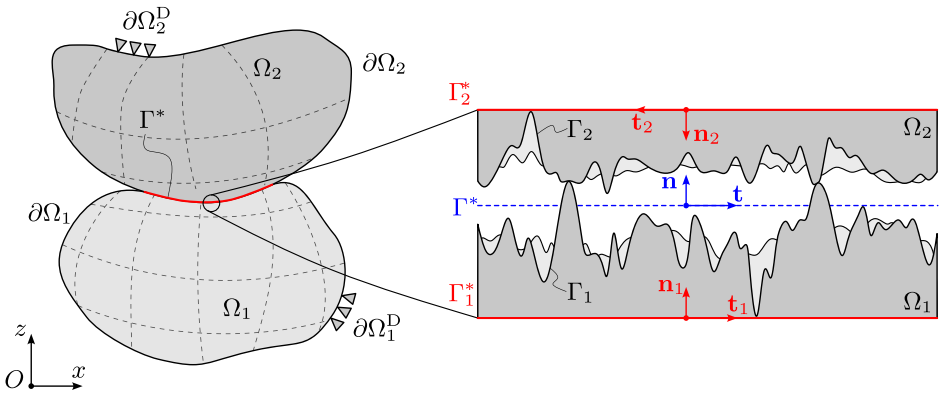

Fig. 2. Solid domains $\Omega_{i=1,2}$ coming into contact at the nominally smooth interface Γ^*.

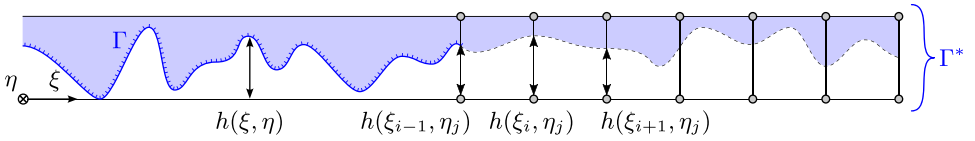

Fig. 3. Nominally smooth interface Γ^* with embedded rough surface defined by the roughness function $h(\xi,\eta)$, and its discretization in MPJR interface finite elements. The embedding operation is shown along one single profile of the 3D surface at a constant coordinate η_j.

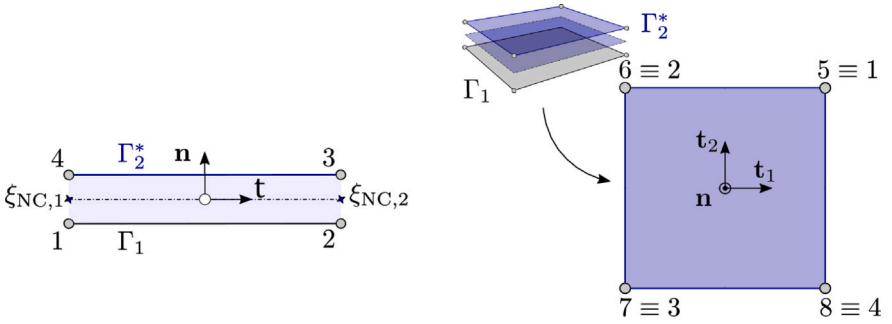

Fig. 4. 2D and 3D interface finite elements. Integration points are coincident with nodes according to Newton–Coates formulae.

correspondence with the coordinates of the same point in the global reference system. The surface elevation is computed with respect to a reference smooth surface parallel to the average plane with datum set in correspondence of its deepest valley, see Fig. 3.

The contact interactions between the solids can be described by the relation between the gap vector $\boldsymbol{g} = [g_n, g_{t1}, g_{t2}]^\intercal$ at the contact interface Γ^* and the contact tractions $\boldsymbol{\tau} = [p_n, \tau_1, \tau_2]^\intercal$. For simplicity, a frictionless contact problem is considered here, focusing on the derivation of the normal components. The frictional contribution can be added to the framework as in [51].

The contact interface contribution to the weak form of the equilibrium equation can be written as:

$$\Pi_{\Gamma^*} = \int_{\Gamma^*} p_n(\mathbf{u})\delta g_n(\mathbf{v})\,\mathrm{d}\Gamma. \tag{1}$$

The numerical solution of the contact problem in the finite element framework requires the discretization of the two bodies and of the contact interface into finite elements. In this work, the bulk has been discretized by linear isoparametric finite elements, even though there is no restriction on the finite element topology, provided that it is consistent with that of the MPJR interface finite elements used, which are represented in Fig. 4 for the 2D and 3D cases.

Introducing a vector of nodal displacements $\mathbf{u} = [u_{x1}, u_{y1}, u_{z1}, \dots, u_{x8}, u_{y8}, u_{z8}]^\intercal$ (in 3D), the gap vector $\boldsymbol{g}$ can be computed as:

$$\boldsymbol{g} = \mathbf{QNLu}, \tag{2}$$

where $\mathbf{L}$ is a linear operator for computing the relative displacements across the interface, $\mathbf{N}$ is the shape functions matrix, and $\mathbf{Q}$ is a rotation matrix for transforming displacements from the global to the local reference frame of the interface finite element (see [49] for the operators' derivation).

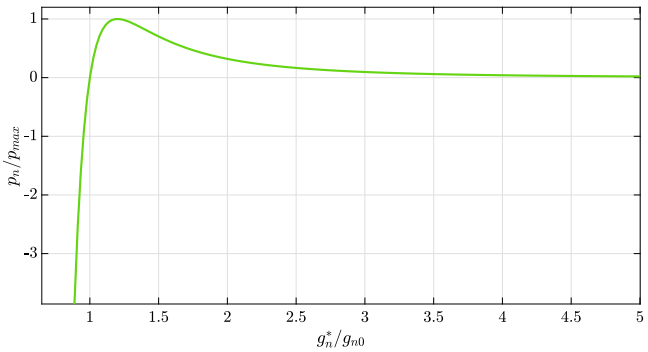

Fig. 5. Traction-relative displacement curve related to the Lennard-Jones potential employed as the interface constitutive law.

The original deviation from planarity between the smoothed and the actual geometry of the contact surface can be restored by a suitable correction of the normal component of the gap: $g_n^* = g_n + h(\xi, \eta)$, where $h(\xi, \eta)$ establishes a one-to-one correspondence between a point on the rough surface in the local and global reference systems.

In the case of AFM data, the surface elevation field is defined as $z_{ij} \equiv h(\xi_i, \eta_j)$, sampled on a Cartesian grid for which, at each scanning point, the equivalence $(x_i, x_j) \equiv (\xi_i, \eta_j)$ holds. This elevation field is introduced in the MPJR finite element considering the corresponding modified normal gap computed at each integration point as:

$$g_n^*(x_i, x_j) = g_n(x_i, x_j) + z_{ij}. \tag{3}$$

Using the modified gap in the derivation of the stiffness matrix of the system allows us to account for the complex geometry without considering it explicitly during the FE discretization process.

When an adhesive contact problem is considered, the constitutive relation in the normal direction can be written using a Lennard-Jones potential-like relationship [56,57]:

$$p_n = \frac{A_N}{6\pi g_0^3}\left[\left(\frac{g_0}{g_n^*}\right)^9 - \left(\frac{g_0}{g_n^*}\right)^3\right] = \frac{8\Delta\gamma}{3g_0}\left[\left(\frac{g_0}{g_n^*}\right)^3 - \left(\frac{g_0}{g_n^*}\right)^9\right], \tag{4}$$

where A_N is the Hamaker constant; g_0 is the equilibrium spacing between the two half-spaces; and $\Delta\gamma$ is the adhesion energy per unit area.

The AFM provides the value of the dissipated energy during an approach-withdrawing cycle of the tip, given by the shaded area in Fig. 1. Under the hypothesis that the area under the approach curve is negligible, the dissipated energy can be exploited to compute the adhesion energy per unit area $\Delta\gamma$. This can be accomplished by dividing the dissipated energy value by the area of the unit cell scanned by the AFM tip, which depends on the resolution chosen for the acquisition.

Similarly, the peak adhesive force $F_{\max}$ measured by the AFM can be used to compute interface tractions. For instance, the maximum adhesive traction, $p_{\max}$, is obtained by dividing $F_{\max}$ by the unit cell area of the AFM measurement. The experimental value of $p_{\max}$ can be exploited to calculate the value of g_0 in Eq. (4) as follows. The stationary point $g_{\max}$ of the equation can be expressed in terms of g_0 as:

$$g_{\max} = \sqrt[6]{3}g_0. \tag{5}$$

If this value is introduced in Eq. (4), then a functional relationship can be derived linking $p_{\max}$ and g_0:

$$g_0 = \frac{16}{9\sqrt{3}}\frac{\Delta\gamma}{p_{\max}}. \tag{6}$$

Finally, this value can be substituted into Eq. (4) to derive a potential that is only a function of $p_{\max}$ and $\Delta\gamma$, that is, the quantities acquired by AFM scan. The very same equation can be expressed as:

$$p_n = -(a_1 g_n^{*b_1} - a_2 g_n^{*b_2}), \tag{7}$$

where:

$$a_1 = 3.284\frac{\Delta\gamma^9}{p_{\max}^8}, \qquad a_2 = 2.809\frac{\Delta\gamma^3}{p_{\max}^2}, \qquad b_1 = -9, \qquad b_2 = -3. \tag{8}$$

The resulting force–displacement curve potential plotted in Fig. 5 is theoretically defined for any value of g_n^*, presenting an asymptote in $g_n^* = 0$. Simulating adhesive contact problems using this model presents several challenges, primarily due to the highly nonlinear nature of the Lennard–Jones relation. One of the main difficulties is the absence of an undeformed equilibrium position for two interacting deformable bodies. According to the model, interaction forces arise as long as the bodies remain within a finite distance, leading to continuous deformation. Another significant challenge is the appearance of attractive instability in cases of

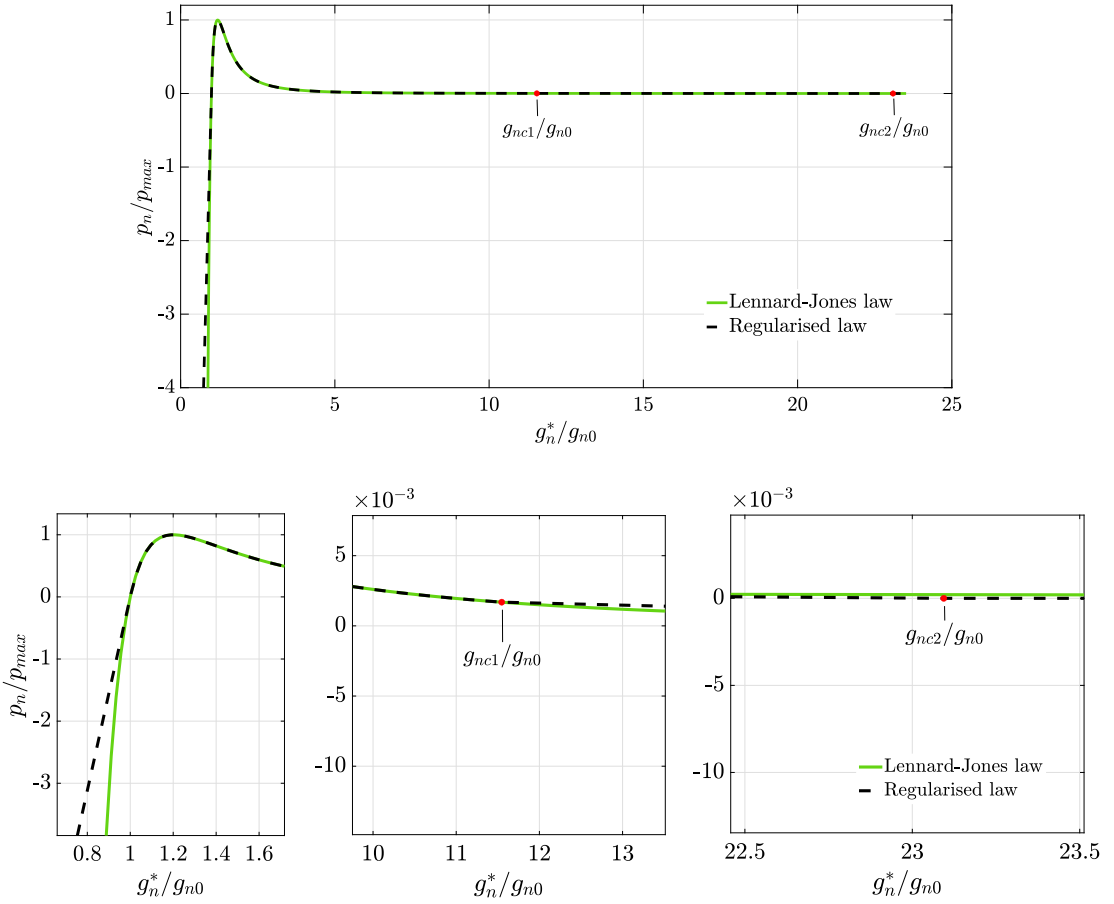

Fig. 6. Regularization of the Lennard-Jones traction–displacement relation for the interface finite element.

strong adhesion. This instability, commonly referred to as jump-to-contact and jump-off-contact, can be particularly problematic in quasi-static simulations. To mitigate this issue, arc-length methods or dynamic simulation techniques can be used [56]. Additionally, the tangent matrix may become ill-conditioned as $g_n^* \to 0$ because the Lennard-Jones relation and the corresponding contact stiffness tend to infinity. This issue is particularly pronounced when large load increments are used or when finite element discretization is too coarse, especially in the presence of strong adhesion, as the contact stiffness scales with A_N. To address this, smaller load increments and finer element discretization can be utilized.

In the present numerical formulation, the relationship in Eq. (7) has been regularized by (i) considering that the adhesive contribution can be neglected for high values of the gap and (ii) removing the asymptote at $g_n^* = 0$. The first regularization approximates the Lennard-Jones curve with a linear law between g_{nc1} and g_{nc2}. These two values have been set by computing analytically the area under the Lennard-Jones curve. The gap value g_{nc1} is set such that the area in the range $[g_{n0}, g_{nc1}]$ is equal to 99% of the total area. The value g_{nc2} is computed by setting the area of the approximating linear branch equal to 1% of the total area. Regarding the asymptote, a linear approximation is introduced: for $g_n^* \leq g_{n0}$, the normal contact traction is computed using the analytical tangent to the Lennard-Jones potential at $g_n^* = g_{n0}$, (noted as k_0). The tangent can be further adjusted to prevent ill-conditioning problems for $g_n^* \to 0$ by multiplying its value with a user-defined factor, denoted as k_t. In the numerical simulations presented in the remainder of the article, k_t is set equal to 10^2 for the whole surface, while k_0 is computed point-wise according to the local values of the adhesive parameters.

The regularized version of the Lennard-Jones constitutive relation (plotted in Fig. 6 as the dashed black line) reads:

$$p_n = \begin{cases} k_t\, k_0\, (g_n^* - g_{n0}) & \text{if} \quad g_n^* \leq g_{n0}, \\ -(a_1 g_n^{*b_1} - a_2 g_n^{*b_2}) & \text{if} \quad g_{n0} < g_n^* \leq g_{nc1}, \\ \dfrac{a_1 g_{nc1}^{b_1} - a_2 g_{nc1}^{b_2}}{g_{nc2} - g_{nc1}} (g_n^* - g_{nc2}) & \text{if} \quad g_{nc1} < g_n^* \leq g_{nc2}, \\ 0 & \text{if} \quad g_n^* > g_{nc2}. \end{cases} \tag{9}$$

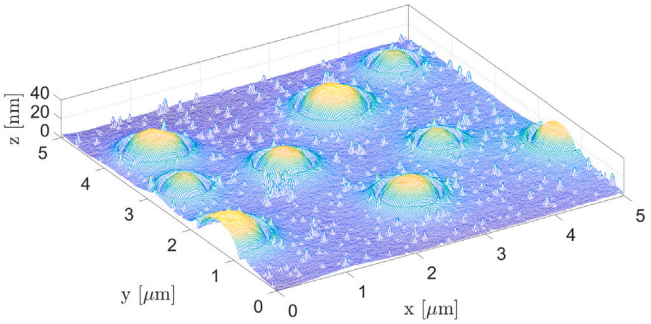

Fig. 7. Height field of the PS-LDPE sample where the LDPE semi-spherical inclusions are clearly visible.

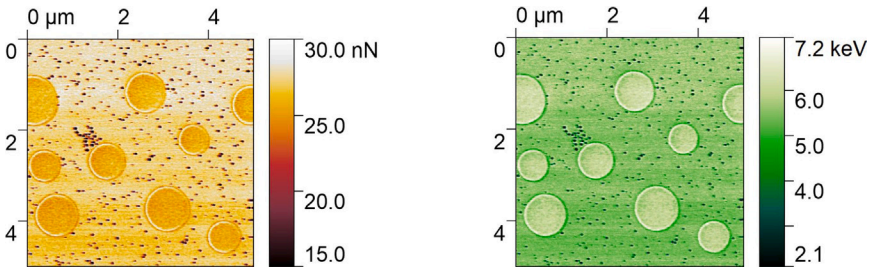

Fig. 8. Adhesive force field on the left, and energy dissipation on the right, for the PS-LDPE sample.

Compared to the analysis of adhesive contact problems in [50], the parameters in Eq. (9) depend on the coordinate of the interface integration point. To minimize access to external files, the surface elevation field and the Lennard-Jones parameters are stored in the finite element routine based on the correspondence between the AFM data spatial coordinates and the coordinates of the interface finite element, using three history variables for each integration point; this operation is done only once at the initialization of the FE simulation.

As in the previous authors' contributions, the interface finite element is coded as a user element in the finite element analysis program FEAP8.6 [58]. A full Newton–Raphson iterative-incremental scheme is employed to solve the nonlinear system of algebraic equations stemming from the FE discretized weak form.

3. 3D adhesive rough contact simulation

The capabilities of the proposed numerical framework are tested in this section using actual experimental data provided by the NEST laboratory of Scuola Normale Superiore (Pisa, Italy) using the BRUKER "DIMENSION ICON" Atomic Force Microscopy (AFM) system, typically employed for characterization of surfaces at the nanoscale.

The material used for the first example consists of a PS-LDPE sample composed of a polystyrene (PS) matrix and low-density polyethylene (LDPE) as a doping component. The morphology of the sample is shown in Fig. 7 and represents a portion of the sample with a scanned surface of 5×5 µm^2 with 256 points per side. The maximum elevation is $h_{\max} = 33$ nm and the root-mean-square of the heights field is $h_{\text{rms}} = 24.8$ nm. The Bruker AFM tips used in the experimental acquisitions have a tip radius of curvature of 25 nm, while the radius of the LDPE inclusions is about 500 nm, much bigger than the tip radius, assuring that the surface morphology is accurately sampled.

The topography has been used in the model without any filtering. The presence of spikes and hard discontinuities on the surface represents a challenge for traditional numerical methods, allowing us to test the real capabilities of the MPJR framework.

The variation of the adhesive peak force and energy dissipation on the sample surface is shown in Fig. 8.

As a benchmark problem to demonstrate the capabilities of the described numerical framework, we simulate the contact problem between the deformable PS-LDPE sample presented above with a rigid flat indenter, as shown in Fig. 9(a). Clearly, this is just one possible contact scenario that can be simulated using FEM and that cannot be inspected using AFM alone and would require other testing machines for larger scale tribological measures. Therefore, the example should be considered as a proof of concept demonstrating the applicability of the proposed methodology to deliver high-fidelity tribological simulations. Under the hypothesis of small displacements and homogeneous material, this problem is equivalent to the case of a rigid rough indenter having the sample height field indenting a deformable substrate with the PS-LDPE mechanical properties, as demonstrated in [59]. The elevation field of the rough indenter has been obtained by computing the composite topography as described in [49] and shown in Fig. 9(b).

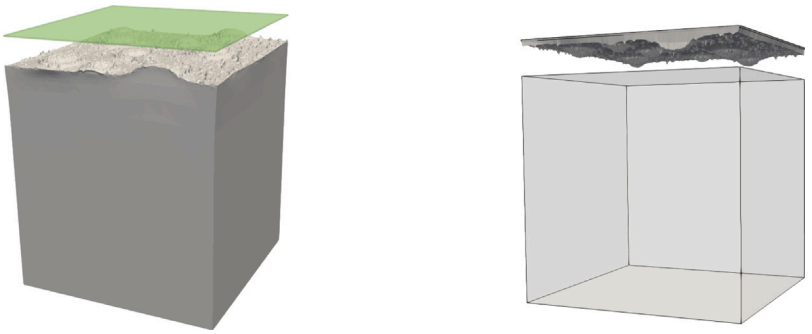

Fig. 9. Benchmark test: contact problem between the PS-LDPE sample and a flat rigid indenter, on the left, and the equivalent problem on the right.

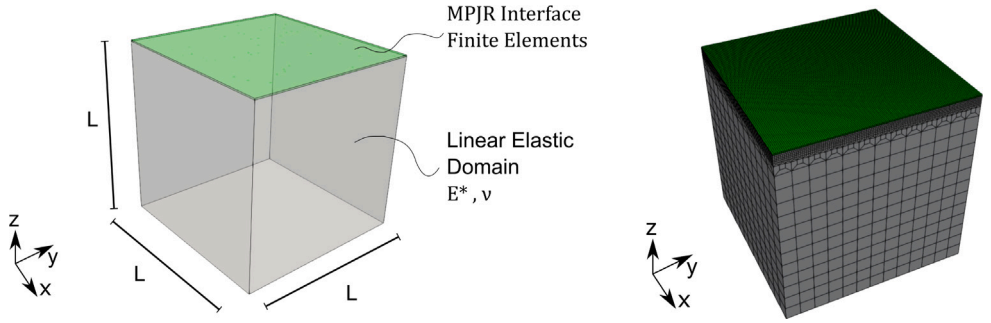

Fig. 10. FE model of the benchmark test. The MPJR interface finite elements fully embed the AFM data of the PS-LDPE sample.

The finite element model, shown in Fig. 10, consists of a deformable cubic domain in contact with the layer of the MPJR interface finite elements, which embeds the real composite topography and the adhesive properties of the PS-LDPE sample.

The cubic domain is discretized using a finer mesh near the contact interface and increasing the size of the finite element mesh at the external part of the domain, as shown in Fig. 10. The interface is discretized with 256×256 MPJR finite elements, which conform to the solid mesh in the refined region near the surface. This discretization has been chosen according to the resolution of the experimental AFM data, avoiding any sub-sampling or smoothing of the rough surface in the numerical model. Therefore, all the available experimental data are embedded in the discretized model, saving the surface height field and the L-J parameters at integration points, which correspond to the interface element nodes. Under this approach, the method would provide the same accuracy as BEM, which introduces a punch-like discretization with elevations taken from the same experimental data; see a detailed comparison in [52] for an adhesiveless contact problem.

The regularized Lennard-Jones relation gives rise to a finite-sized adhesive process zone which can be computed as $l_{\text{ad}} = E^* G_c/\sigma_c^2$, where, in this contest, G_c corresponds to the dissipated energy per unit area and σ_c is the peak adhesive traction. Considering the average values of the parameters employed in the model, the process zone length is equal to 5.77×10^{-8} m. Based on the above surface discretization, the element size h_e is 0.975×10^{-8} m. The ratio $h_e/l_{\text{ad}} = 0.17 \ll 1$ ensures that the adhesive process zone is sufficiently well-discretized. Since h_e matches the experimental sampling interval, the above issue translates to how the surface is experimentally acquired. An experimentalist should be guided by the value of l_{ad} to acquire the surface with an appropriate fine sampling such that the distance between two measured points is much less than l_{ad}, to capture the topological features responsible for adhesion.

The boundary conditions consist of fixing the degrees of freedom of the upper surface of the indenter and applying an upward vertical displacement to the lower surface of the substrate. No constraints are introduced on the free lateral surfaces of the elastic bulk. This is a typical situation where the specimen is fixed on the sample holder through pneumatic vacuum. The finite element method gives the full flexibility to consider also other types of lateral constraints, as e.g. periodic boundary conditions, and compare the effect of different assumptions.

In this first benchmark test, the PS-LDPE sample is treated as a linear elastic homogenized material, assuming an effective elastic modulus estimated according to a simple mixture-rule, denoted with E^*, calculated from the values measured by the AFM. The experimental data show that the LDPE elastic modulus is lower than that of PS due to the olefin structure in the molecule chain, as shown in Fig. 11 in terms of DMT elastic modulus. The average DMT modulus for the two phases has been calculated from the AFM data: $E_{\text{PS}} = 132.03$ MPa and $E_{\text{LDPE}} = 66.88$ MPa. The effective value has been obtained by considering volumetric ratios of the two phases $V_{\text{PS}} = 0.85$ and $V_{\text{LDPE}} = 0.15$ as follows:

$$E^* = \frac{V_{\text{LDPE}}}{V_{\text{LDPE}} + V_{\text{PS}}} E_{\text{LDPE}} + \frac{V_{\text{PS}}}{V_{\text{LDPE}} + V_{\text{PS}}} E_{\text{PS}} = 121.76\,\text{MPa}. \tag{10}$$

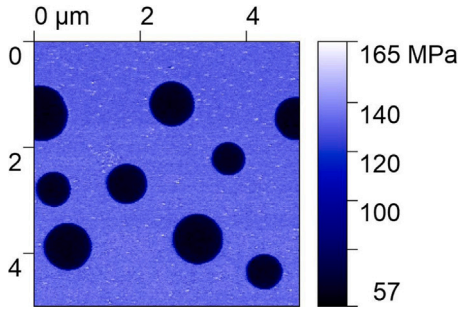

Fig. 11. Spatial variation of the DMT elastic modulus of the PS-LDPE sample.

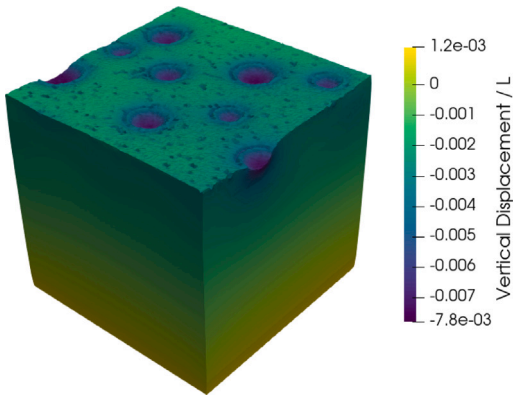

Fig. 12. Deformed configuration of the sample (the deformation is magnified 10× for visualization purposes) for a vertical displacement of $0.25h_{\text{rms}}$ applied to the PS-LDPE sample which is pushed against the rough surface.

The volumetric ratios have been estimated by assuming that the surface composition given by the AFM scan corresponds to the volume percentage in the bulk. The Poisson ratio is set equal to $\nu = 0.32$ as in [60] for a PS-LDPE blend of similar composition.

The simulated quantities, including the heights, adhesion, and dissipated energy used as input for the interface, have been normalized using the lateral size of the simulated sample, $L = 5\,\mu\text{m}$, and the effective elastic modulus, E^*.

The simulation results for an applied displacement along the z-axis equal to $0.25h_{\text{rms}}$ are shown in the contour plot of the vertical displacements u_z/L, Fig. 12. The effect of the PS-LDPE height field and the L-J repulsive forces can be seen on the indented surface.

The results of the described numerical framework have been compared with those obtained by neglecting the adhesion contribution, considering a simpler penalty approach where the penalty stiffness has been set constant over the whole surface and equal to the average value of the above experimentally evaluated penalty coefficients. For the analyzed PS-LDPE sample, the average penalty stiffness k_0 results equal to $97.7\,E^*/L$. This value, multiplied by the numerical factor $k_t = 100$ as described in the previous section, has been used for the simpler adhesiveless model to be compared with the adhesive model having a point-wise variability of the penalty stiffness over the surface derived from the AFM sampling.

The comparison of the resulting dimensionless normal traction is shown in Fig. 13 for two interface cross-sections in directions x and y. The model considering the Lennard-Jones force–displacement relation is characterized by regions having positive tractions (adhesion) and higher negative tractions caused by the repulsive forces between the surfaces.

As previously described, the proposed modeling approach includes an interface constitutive law point-wise defined according to the field data collected with the AFM. The effect of considering a spatially varying adhesive relation over the surface is highlighted in Fig. 14 where the simulation results have been compared with those of the same simulation but considering a homogeneous constitutive law whose parameters for the Lennard-Jones relationship are set equal to the average values provided by the experimental results over the whole surface. In this case, the bottom surface of the PS-LDPE has been fixed, while a vertical displacement $\bar{u}_z = 0.2h_{rms}$ is applied to the indenter surface, corresponding to moving away the indenter from the substrate. While the contact stress variation depends only on the surface roughness in the homogeneous case, the point-wise defined constitutive law allows the simulation of the combined effect of adhesion and roughness.

4. Assessing the role of the bulk heterogeneity

In the previous section, the sample was considered as a homogeneous linear elastic material with an effective (homogenized) elastic modulus and heterogeneous interface properties. In this section, we remove the simplification of a homogenized continuum,

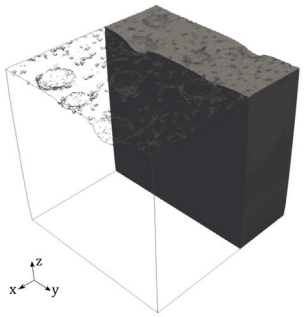

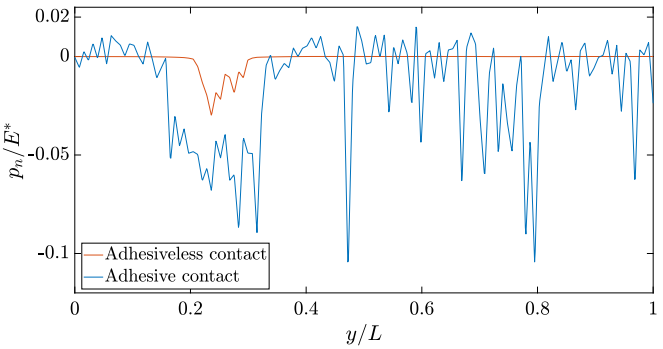

(a) Section normal to the axis y, at $x = 0.38L$

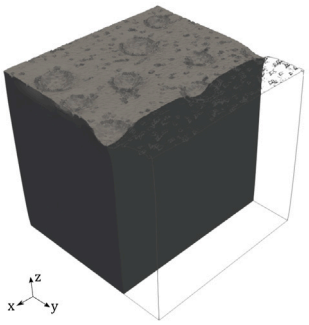

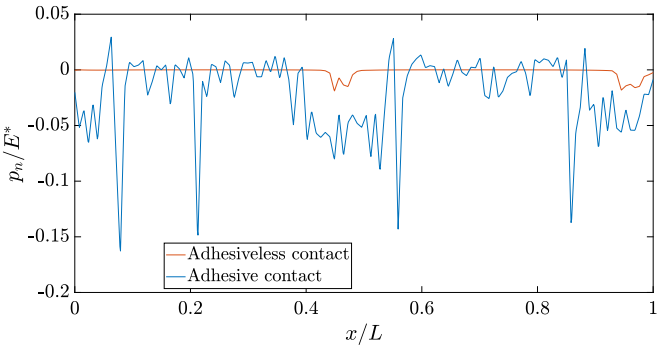

(b) Section normal to the axis x, at $y = 0.75L$

Fig. 13. Comparison of the dimensionless normal traction σ_n/E^* at two chosen interface sections, with or without the adhesive law. Imposed far-field displacement to the bottom surface of the PS-LDPE sample $\bar{u} = 0.25h_{\text{rms}}$.

and we investigate the effect on the contact response of using dissimilar elastic properties in the bulk, since, for the present heterogeneous sample, the AFM technique provides an accurate map of the bulk elasticity from surface measures. Hence, different elastic moduli for the two polymeric phases of the PS-LDPE sample are considered.

For this simulation, a single rough profile has been extracted from the surface topology as shown in Fig. 15 and imported in the 2D interface finite elements, together with the corresponding values of maximum adhesion force and energy dissipation at each profile coordinate.

The geometry of the FE model is depicted in Fig. 16. Compared to the 3D model of the previous section, the 2D model thickness t has been set equal to 0.2 μm, considering that the PS-LDPE layer is deposited on a silicon substrate, which can be treated as rigid because its Young's modulus is ≈ 150 GPa, much higher than those of the polymeric components. For this reason, the discretization of the silicon substrate layer has been neglected, and the polymeric layer has been constrained at the bottom edge, again due to pneumatic vacuum that fixes the sample on the sample holder.

Fig. 16 also shows how the two polymeric phases alternate in the sample. This variation can be recognized by looking at the elastic modulus values measured with the AFM along the chosen profile and depicted in Fig. 17. The threshold value of 72.44 MPa (represented as a red line in the figure) has been used to distinguish between the two components along the x direction, and the following values of the elastic moduli have been set: (i) $E_1 = E_{\text{PS}} = 128.67$ MPa for the PS material model, (ii) $E_2 = E_{\text{LDPE}} = 64.27$ MPa for the LDPE.

The simulation has been conducted by prescribing a non-monotonic far-field displacement path to the indenter, composed of two ramps throughout the pseudo-time evolution. In the first ramp (denominated approaching ramp), the rough indenter is pushed against the polymeric layer, increasing the imposed far-field displacement $\bar{u}$ up to $\bar{u} = -3h_{\text{rms}}$. Then, the far-field displacement is reverted until the two surfaces are pulled apart (denoted as separation ramp). The displacement path is represented in Fig. 18.

Fig. 19 depicts the normal contact tractions during the simulation. For visualization purposes, the interface response has been represented in three separate plots: Fig. 19(a) corresponds to the approach ramp; Fig. 19(b) shows the contact tractions from the beginning of the separation ramp to the time-step when the maximum adhesive force is achieved (corresponding to $\bar{u} = 6.7h_{\text{rms}}$ and $P = 0.24$N); Fig. 19(c) represents the decrease in the contact tractions from the maximum adhesive force to almost complete separation of the two surfaces, showing that detachment does not occur simultaneously along the interface. First, it happens in the PS regions, and later, the LDPE inclusions also detach from the indenter, which is consistent with the adhesive data collected by the AFM (see Fig. 8) where the PS matrix has, on average, a lower value of the maximum adhesive force.

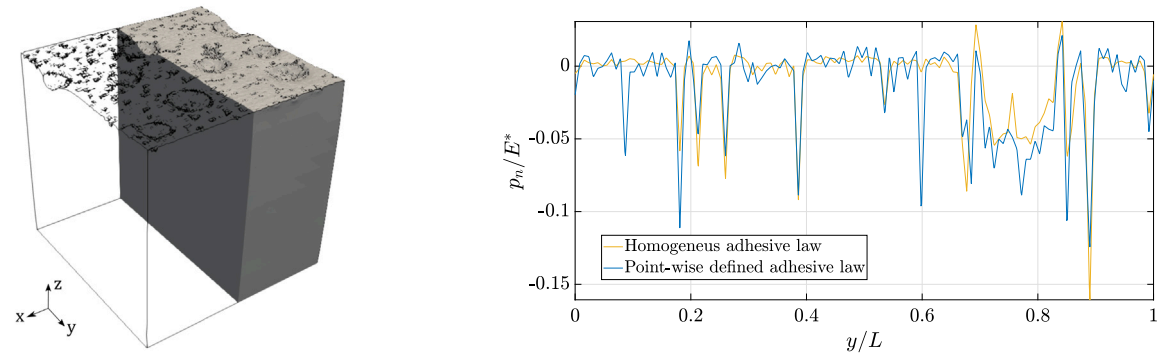

(a) Section normal to the axis y, at $x = 0.5L$

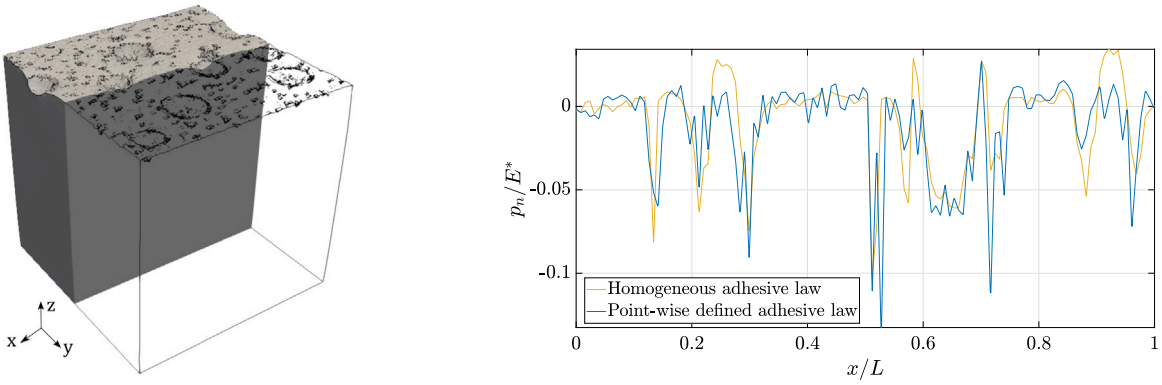

(b) Section normal to the axis x, at $y = 0.5L$

Fig. 14. Comparison of σ_n/E^* at two chosen interface sections for the model having the coefficients of the interface constitutive law defined point-wise according to the ATM data, versus the model using homogeneous, averaged coefficients over the whole surface. Imposed far-field displacement $\bar{u}_z = 0.2h_{\text{rms}}$ (the indenter is pull-out from the sample).

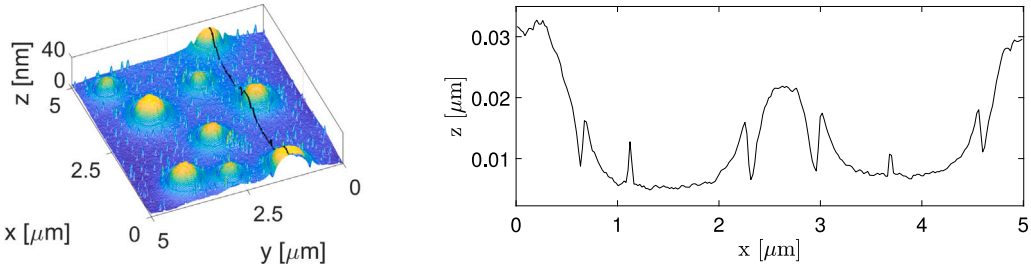

Fig. 15. PS-LDPE profile extracted from the surface topography, for the 2D simulations.

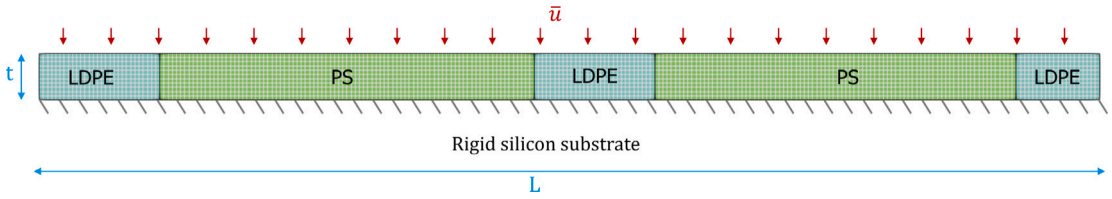

Fig. 16. 2D geometry and boundary conditions of the sample showing the two polymeric phases, PS and LDPE. The sample thickness is $t = 0.2$ μm, and the length is $L = 5$ μm.

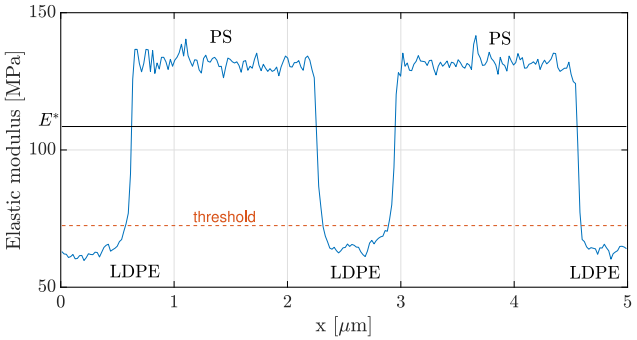

Fig. 17. Elastic modulus variation along the analyzed profile. The red dashed line shows the threshold chosen to separate the PS and the LDPE phases; the black continuum line corresponds to the value of homogenized elastic modulus $E^* = 108.5$ MPa we used in the homogenized model of the continuum.

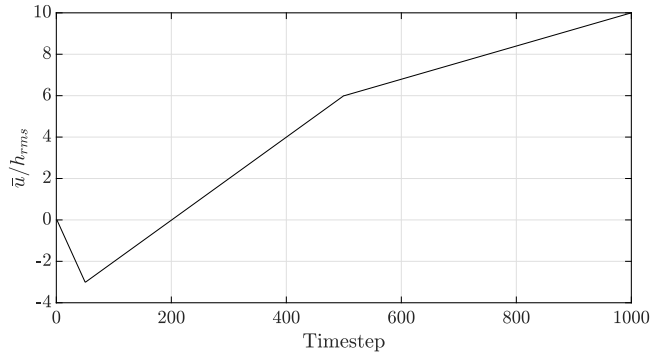

Fig. 18. Imposed far-field displacement $\bar{u}$ applied to the top edge of the indenter with respect to a pseudo-time variable. After the first approaching stage, the indenter is pulled out from the substrate.

The total resulting reaction force is plotted in Fig. 20 with respect to the applied displacement. As expected, the reaction force during the approaching ramp overlaps with the initial part of the separation ramp since the energy dissipation during the approach stage has been neglected when computing the interface constitutive law. Moreover, after reaching the maximum adhesive force, the total reaction force shows a snapback instability. The full Newton–Raphson algorithm assures a very fast convergence up to the peak force with about two iterations per loading step and afterward requires hundreds of iterations due to the strong instability. The arc-length control scheme could be exploited to deal with the unstable snapback branch that cannot be captured under displacement control.

The instabilities related to adhesive contact problems have been intensively studied in the literature (see, e.g., [5,38,61,62] and references therein). The traction law in Eq. (4) can be regarded as a nonlinear spring in series with the linear spring associated with the deformable substrate (assuming a rigid indenter) having stiffness k, which can be assumed equal to E/t, where E is the elastic modulus and t is the substrate depth in the undeformed configuration. This phenomenon is analogous to the case of a nonlinear interface law with softening behavior studied in [63]. That work can be used as a guideline to identify the occurrence of instabilities for the proposed Lennard-Jones-like constitutive law exploited in the present work. In fact, instabilities can appear when:

$$\left|\frac{\partial p_n}{\partial g_n}\right|_{\max} > \frac{E}{t} \tag{11}$$

where $\left|\frac{\partial p_n}{\partial g_n}\right|_{\max}$ is the maximum module of the tangent of the interface constitutive law. Considering the average values of the interface parameters used for the PS-LDPE example, the tangent maximum value is $|\partial p_n/\partial g_n|_{\max} = 2.17 \times 10^6$ N/mm^3. Using $t = 0.0002$ mm (substrate depth) and $E = 108.5$ MPa, we obtain $E/t = 5.427 \times 10^5$ N/mm^3. Hence, the present situation satisfies the inequality in Eq. (11), which confirms the occurrence of instabilities revealed in the reaction force–displacement curve.

The present case can be compared with another hypothetical situation where the interface properties are the same, while the elastic moduli of the two components are assumed to be two orders of magnitude higher than before: (*i*) $E_1 = 12867$ MPa for the first phase, (*ii*) $E_2 = 6427$ MPa for the second phase. The above inequality is not satisfied for this case since $E/t = 5.427 \times 10^7$ N/mm^3. The different behavior is confirmed by the simulation results plotted in Fig. 21 where no instabilities are observed.

In case of a sphere in contact with a half-plane, the present case leading to instability would also be expected by a criterion based on the value of the Tabor parameter [5,64]. The Tabor parameter is inversely proportional to the elastic modulus. Hence, for lower values of the elastic modulus, the contact problem tends to behave according to the Johnson–Kendall–Roberts (JKR) model [65] characterized by a *S-shaped* force–displacement curve.

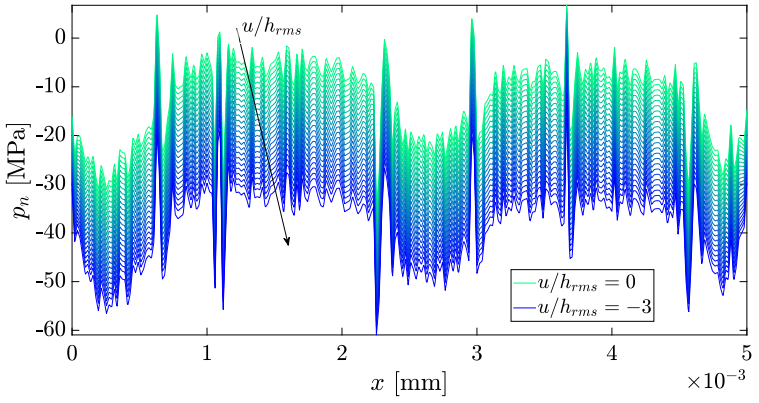

(a) Approach ramp.

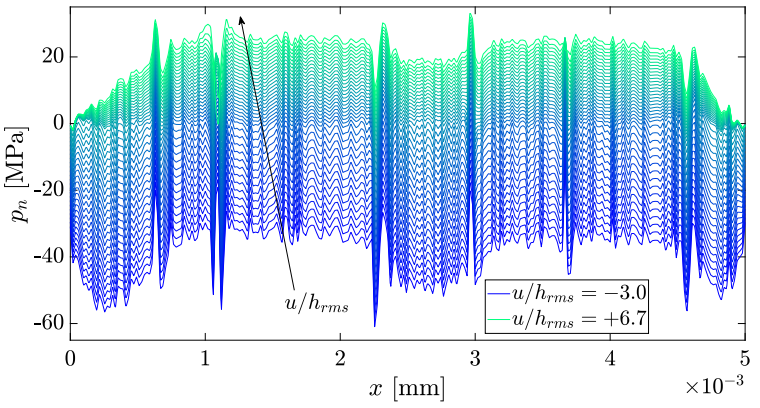

(b) Separation stage up to the adhesive peak force.

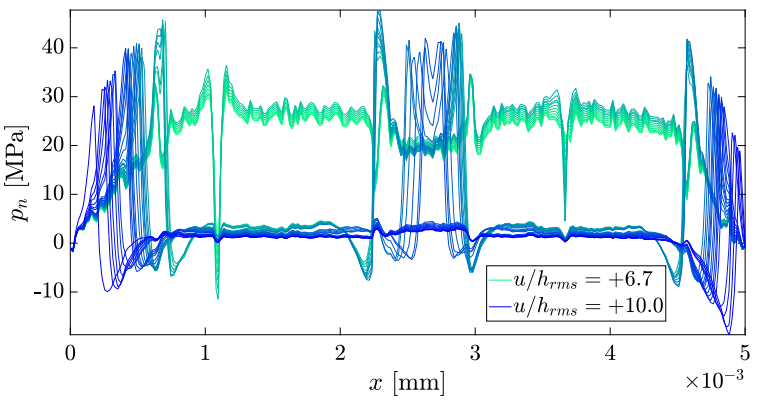

(c) Separation stage from the adhesive peak force to almost complete detachment.

Fig. 19. Contact tractions variation during the approach ramp (a) and in the following separation stage (b–c). The total reaction force increases till the maximum adhesive force, corresponding to an imposed far-field displacement $\bar{u} = 6.7h_{\text{rms}}$ in (b), and decreases to almost zero in (c).

As a remark, in case of thicker layers or half-spaces, refined stability analyses would be required. As shown in [66], the interaction between asperities can increase due to long-range elastic interactions, and this would need to consider non-local stability criteria.

In order to demonstrate the versatility of the MPJR approach for heterogeneous contact problems, the present model results have been compared to the homogenized simulation, where the elastic modulus of the bulk is set equal to the effective (homogenized) value 108.5 MPa for the PS and LDPE phases, computed according to Eq. (10) based on the volumetric ratios selected for the chosen

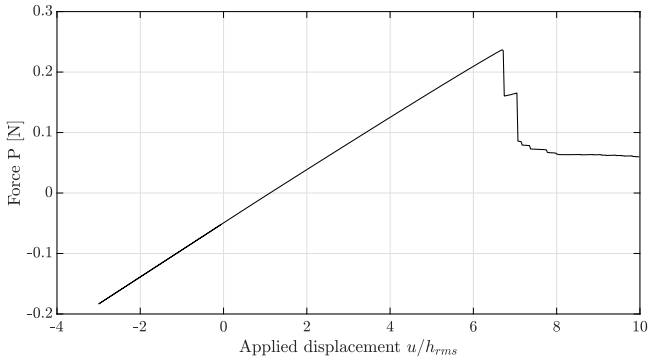

Fig. 20. Total reaction force vs. the imposed far-field displacement for the 2D model with the heterogeneous substrate, alternating the PS and the LDPE phases as in the real sample.

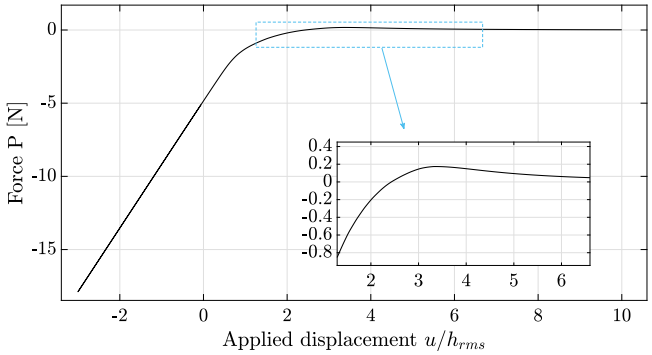

Fig. 21. Total reaction force vs. applied displacement for an exemplary case with elastic moduli two orders of magnitude bigger than in Fig. 20. This case does not show snapback instabilities.

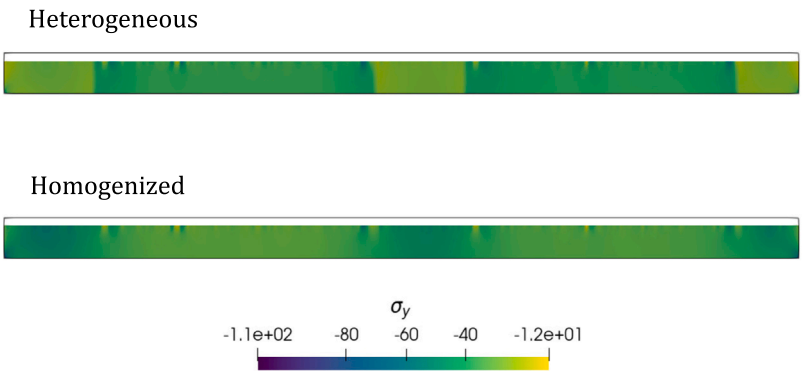

Fig. 22. Contour plot of σ_y resulting from the homogenized model having elastic modulus E^* and in the case of the model with two different elastic modulus values for the PS and LDPE phases, for an imposed displacement of $\bar{u} = -3h_{rms}$.

profile. The heterogeneous and homogenized simulations are compared in Fig. 22 in terms of contour plots of the stress component σ_y for an imposed displacement of $\bar{u} = -3h_{rms}$. The heterogeneous model clearly shows the difference between the two material phases. Moreover, the value of σ_n in the two cases is shown in Fig. 23 for the same applied displacement.

Finally, the reaction forces for the two cases are shown in Fig. 24. It can be noticed that, even though the two simulations refer to the same spatial distributions of the mechanical properties over the surface taken from AFM data, bulk homogenization performs well in predicting the global average stiffness, which is coincident with the heterogeneous solution, while it gives a higher maximum force. This result shows the importance of including the material heterogeneity not only in the adhesive contact models but also in the bulk, and provides a proof of concept on the possibility of using AFM local stiffness maps to generate realistic heterogeneous models.

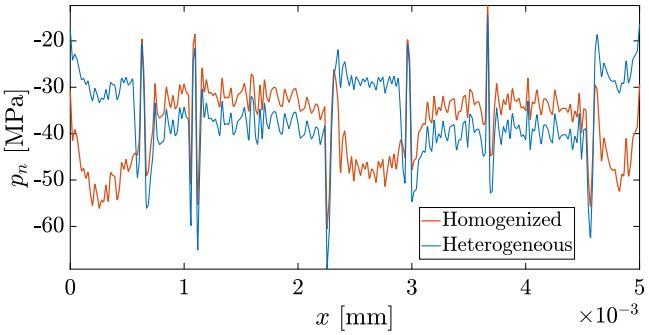

Fig. 23. Contact traction p_n resulting from the homogenized model having elastic modulus E^*, and the heterogeneous model with two different elastic modulus values for the PS and LDPE phases, for an imposed displacement of $\bar{u} = -3h_{rms}$.

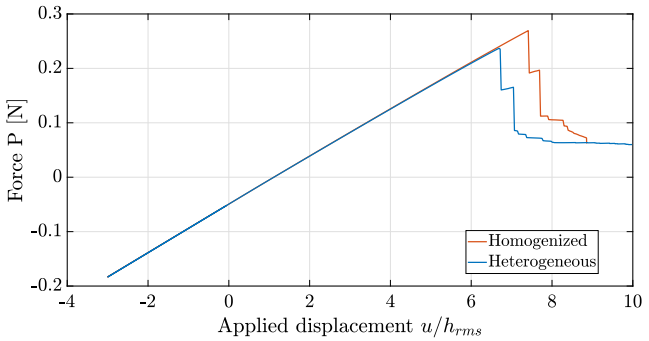

Fig. 24. Comparison of the total reaction force vs. the imposed far-field displacement for the simulations with the effective elastic modulus E^* (homogenized case), and with two different elastic moduli for the PS and LDPE phases (heterogeneous case).

5. Conclusion

This study extended the MPJR interface finite element developed in previous works [49,50,52] and established in the first part of the article a method that fully incorporates experimental data from Atomic Force Microscope (AFM) into the finite element method for high-fidelity contact mechanics simulations, particularly for adhesive rough contacts.

In the second part of the article, focusing on a real PS-LDPE sample with alternated phased, it has been shown that the high-resolution AFM experimental data can be successfully incorporated into 2D and 3D finite element models to solve the underlying complex contact problem. The simulations have been performed in relation to a rigid indenter acting on the whole rough surface, as a proof of concept of any possible tribological test that cannot be performed using AFM alone and that would require other testing machines. Thus, the method proved to be effective in bridging the gap between AFM nanoscale characterization and FE global mechanical simulations towards tribological simulations of industrial interest.

Specifically, it has been shown that integrating spatially varying adhesion properties directly obtained from AFM measurements into the numerical model provides a more realistic and physically accurate representation of rough surface interactions at the micro- and nanoscales. Considering the actual surface topography along with adhesion and dissipation maps measured by the AFM, without the need for any interpolation or other data pre-processing operation, significant differences have been noticed with respect to the same contact predictions based on average –spatially homogeneous– adhesive properties.

Finally, it has been shown how to exploit AFM data on local stiffness measurements to generate high-fidelity heterogeneous bulk models, distinguishing between the different polymeric phases. The 2D contact mechanics comparison between the heterogeneous model with longitudinally alternated polymeric phases and the homogenized layer led to meaningful differences, which shows that also bulk heterogeneities should be modeled and considered with a great deal of attention in addition to the interface properties.

The analysis of other forms of spatial heterogeneities in the substrate and the use of higher-order homogenization techniques to deal with the issue of scale separation are future directions of research worth being investigated in the area of homogenization mediated by contact mechanics.

In conclusion, the proposed methodology significantly advances adhesive contact modeling, bridging the gap between experimental surface characterization from physicists and material scientists and numerical simulation from experts in computational contact mechanics. Forthcoming studies would encompass the corresponding formulation to geometrically nonlinear and frictional effects. Beyond its immediate application to adhesive rough contact problems, this methodology offers a versatile computational framework for studying a broad range of interface phenomena in tribology, material science, and nanotechnology. The MPJR framework is

promising for the study of phenomena where surface roughness plays a key role, as in wear problems, designing surface topography, fracture induced by repeated application of contact loads, tire-asphalt interaction, nanoscale tribological tests based on AFM data, and multi-field tribological problems.

CRediT authorship contribution statement

M.R. Marulli: Writing – review & editing, Writing – original draft, Visualization, Validation, Software, Methodology, Investigation, Formal analysis, Data curation, Conceptualization. **J. Bonari:** Writing – review & editing, Writing – original draft, Software, Methodology, Investigation, Data curation. **P. Pingue:** Writing – review & editing, Writing – original draft, Resources, Investigation, Data curation, Conceptualization. **M. Paggi:** Writing – review & editing, Writing – original draft, Supervision, Resources, Methodology, Investigation, Formal analysis, Conceptualization.

Declaration of competing interest

The authors declare that they have no known competing financial interests or personal relationships that could have appeared to influence the work reported in this paper.

Acknowledgement

The H2020 Marie Sklodowska-Curie Staff Exchanges project DIAGONAL –Ductility and Fracture Toughness Analysis of Functionally Graded Materials– (GA 101086342) is gratefully acknowledged.

Data availability

Data will be made available on request.

References

[1] A.I. Vakis, V.A. Yastrebov, J. Scheibert, L. Nicola, D. Dini, C. Minfray, A. Almqvist, M. Paggi, S. Lee, G. Limbert, J.F. Molinari, G. Anciaux, R. Aghababaei, S. Echeverri Restrepo, A. Papangelo, A. Cammarata, P. Nicolini, C. Putignano, G. Carbone, S. Stupkiewicz, J. Lengiewicz, G. Costagliola, F. Bosia, R. Guarino, N.M. Pugno, M.H. Müser, M. Ciavarella, Modeling and simulation in tribology across scales: An overview, Tribol. Int. 125 (2018) 169–199.
[2] I.G. Goryacheva, M. Paggi, V.L. Popov, Editorial: Contact mechanics perspective of tribology, Front. Mech. Eng. 7 (2021) 1–5.
[3] M. Paggi, Emergent properties from contact between rough interfaces, in: Marco Paggi, David Hills (Eds.), Modeling and Simulation of Tribological Problems in Technology, Springer International Publishing, 2020, pp. 179–227.
[4] L. Pastewka, M.O. Robbins, Contact between rough surfaces and a criterion for macroscopic adhesion, Proc. Natl. Acad. Sci. USA 111 (9) (2014) 3298–3303.
[5] M. Ciavarella, J. Joe, A. Papangelo, J.R. Barber, The role of adhesion in contact mechanics, J. R. Soc. Interface 16 (151) (2019).
[6] K. Komvopoulos, Adhesion and friction forces in microelectromechanical systems: mechanisms, measurement, surface modification techniques, and adhesion theory, J. Adhes. Sci. Technol. 17 (4) (2003) 477–517.
[7] Animangsu Ghatak, L. Mahadevan, Jun Young Chung, Manoj K. Chaudhury, Vijay Shenoy, Peeling from a biomimetically patterned thin elastic film, Proc. R. Soc. Lond. Ser. A Math. Phys. Eng. Sci. 460 (2049) (2004) 2725–2735.
[8] A.V. Spuskanyuk, R.M. McMeeking, V.S. Deshpande, E. Arzt, The effect of shape on the adhesion of fibrillar surfaces, Acta Biomater. 4 (6) (2008) 1669–1676.
[9] A.B.C. Buskermolen, T. Ristori, D. Mostert, M.C. van Turnhout, S.S. Shishvan, S. Loerakker, N.A. Kurniawan, V.S. Deshpande, C.V.C. Bouten, Cellular contact guidance emerges from gap avoidance, Cell Rep. Phys. Sci. 1 (5) (2020) 100055.
[10] A. Ippolito, V.S. Deshpande, Contact guidance via heterogeneity of substrate elasticity, Acta Biomater. 163 (2023) 158–169, The Mechanics of Cells and Fiber.
[11] H. Kesari, A.J. Lew, Effective macroscopic adhesive contact behavior induced by small surface roughness, J. Mech. Phys. Solids 59 (12) (2011) 2488–2510.
[12] J. Joe, M.D. Thouless, J.R. Barber, Effect of roughness on the adhesive tractions between contacting bodies, J. Mech. Phys. Solids 118 (2018) 365–373.
[13] C. Putignano, L. Afferrante, G. Carbone, G. Demelio, The influence of the statistical properties of self-affine surfaces in elastic contacts: A numerical investigation, J. Mech. Phys. Solids 60 (5) (2012) 973–982.
[14] R.R. Zhao, K.T. Turner, J.L. Bassani, Exploiting interface patterning for adhesion control, J. Mech. Phys. Solids 160 (2022) 104740.
[15] A. Sanner, N. Kumar, A. Dhinojwala, Tevis D.B.J., L. Pastewka, Why soft contacts are stickier when breaking than when making them, Sci. Adv. 10 (10) (2024) 1–7.
[16] T. Andersson, B.G. Allan-Persson, The boundary element method applied to two-dimensional contact problems, in: Progress in Boundary Element Methods, vol. 2, Springer New York, New York, NY, 1983, pp. 136–157.
[17] Yang Xu, R.L. Jackson, Boundary element method (BEM) applied to the rough surface contact vs BEM in computational mechanics, Friction 7 (4) (2019) 359–371.
[18] M. Paggi, A. Bemporad, J. Reinoso, Computational methods for contact problems with roughness, in: CISM International Centre for Mechanical Sciences, Courses and Lectures, vol. 593, Springer International Publishing, 2020, pp. 131–178.
[19] C. Putignano, L. Afferrante, G. Carbone, G. Demelio, A new efficient numerical method for contact mechanics of rough surfaces, Int. J. Solids Struct. 49 (2) (2012) 338–343.
[20] M.R. Marulli, G. Sorrentino, M. Paggi, Multi-scale contact mechanics framework for upper palaeolithic ground stone tools, J. Archaeol. Sci.: Rep. 61 (2025) 104939.
[21] H. Moulinec, P. Suquet, A numerical method for computing the overall response of nonlinear composites with complex microstructure, Comput. Methods Appl. Mech. Engrg. 157 (1998) 69–94.
[22] H. Moulinec, P. Suquet, Comparison of FFT-based methods for computing the response of composites with highly contrasted mechanical properties, Phys. B 338 (2003) 58–60.

[23] S. Liu, X. Jin, Z. Wang, L.M. Keer, Q. Wang, Analytical solution for elastic fields caused by eigenstrains in a half-space and numerical implementation based on FFT, Int. J. Plast. 35 (2012) 135–154.
[24] Yin Chen, Mengqi Zhang, J.Q. Wang, Analysis of adhesive contact of heterogeneous elastic materials, Int. J. Mech. Sci. 266 (2024) 108986.
[25] C. Jacq, D. Nelias, G. Lormand, D. Girodin, Development of a three-dimensional semi-analytical elastic–plastic contact code, J. Tribol. 124 (2002) 653–667.
[26] D. Nélias, V. Boucly, M. Brunet, Elastic–plastic contact between rough surfaces: proposal for a wear or running-in model, J. Tribol. 128 (2006) 236–244.
[27] V. Boucly, D. Nelias, S. Liu, Q.J. Wang, L.M. Keer, Contact analyses for bodies with frictional heating and plastic behavior, J. Tribol. 127 (2005) 355–364.
[28] D. Nélias, E. Antaluca, V. Boucly, S. Cretu, A three-dimensional semianalytical model for elastic–plastic sliding contacts, J. Tribol. 129 (2007) 761–771.
[29] W.W. Chen, S. Liu, Q.J. Wang, Fast Fourier transform based numerical methods for elasto-plastic contacts of nominally flat surfaces, J. Appl. Mech. Trans. ASME 75 (2008) 110221–1102211.
[30] S. Liu, Q.J. Wang, A three-dimensional thermomechanical model of contact between non-conforming rough surfaces, J. Tribol. 123 (2001) 17–26.
[31] K. Zhou, L.M. Keer, Q.J. Wang, Semi-analytic solution for multiple interacting three-dimensional inhomogeneous inclusions of arbitrary shape in an infinite space, Internat. J. Numer. Methods Engrg. 87 (2011) 617–638.
[32] J. Leroux, B. Fulleringer, D. Nelias, Contact analysis in presence of spherical inhomogeneities within a half-space, Int. J. Solids Struct. 47 (2010) 3034–3049.
[33] K. Zhou, H.J. Hoh, X. Wang, L.M. Keer, J.H.L. Pang, B. Song, Q.J. Wang, A review of recent works on inclusions, Mech. Mater. 60 (2013) 144–158.
[34] K. Zhou, W.W. Chen, L.M. Keer, X. Ai, K. Sawamiphakdi, P. Glaws, Q.J. Wang, Multiple 3D inhomogeneous inclusions in a half space under contact loading, Mech. Mater. 43 (2011) 444–457.
[35] S. Medina, D. Dini, A numerical model for the deterministic analysis of adhesive rough contacts down to the nano-scale, Int. J. Solids Struct. 51 (14) (2014) 2620–2632.
[36] V.L. Popov, R. Pohrt, Q. Li, Strength of adhesive contacts: Influence of contact geometry and material gradients, Friction 5 (3) (2017) 308–325.
[37] V. Rey, G. Anciaux, J.-F. Molinari, Normal adhesive contact on rough surfaces: efficient algorithm for fft-based bem resolution, Comput. Mech. 60 (1) (2017) 69–81.
[38] A. Sanner, L. Pastewka, Crack-front model for adhesion of soft elastic spheres with chemical heterogeneity, J. Mech. Phys. Solids 160 (2022) 104781.
[39] C. Putignano, G. Carbone, D. Dini, Mechanics of rough contacts in elastic and viscoelastic thin layers, Int. J. Solids Struct. 69–70 (2015) 507–517.
[40] N. Menga, C. Putignano, G. Carbone, Recent advancements in the tribological modelling of rough interfaces, Machines 10 (12) 2022.
[41] L. Pei, S. Hyun, J.F. Molinari, Mark.O. Robbins, Finite element modeling of elasto-plastic contact between rough surfaces, J. Mech. Phys. Solids 53 (2005) 2385–2409.
[42] R. Buczkowski, M. Kleiber, Elasto-plastic statistical model of strongly anisotropic rough surfaces for finite element 3d-contact analysis, Comput. Methods Appl. Mech. Engrg. 195 (37) (2006) 5141–5161, John H. Argyris Memorial Issue. Part I.
[43] J. Reinelt, P. Wriggers, Multi-scale approach for frictional contact of elastomers on rough rigid surfaces, Comput. Methods Appl. Mech. Engrg. 198 (2009) 1996–2008.
[44] V.A. Yastrebov, J. Durand, H. Proudhon, G. Cailletaud, Rough surface contact analysis by means of the Finite Element Method and of a new reduced model, Comptes Rendus - Mec. 339 (7–8) (2011) 473–490.
[45] P. Wagner, P. Wriggers, C. Klapproth, C. Prange, B. Wies, Multiscale fem approach for hysteresis friction of rubber on rough surfaces, Comput. Methods Appl. Mech. Engrg. 296 (2015) 150–168.
[46] H. Radhakrishnan, S. Akarapu, Two-dimensional finite element analysis of elastic adhesive contact of a rough surface, Sci. Rep. 10 (1) (2020) 1–9.
[47] L. Afferrante, G. Violano, D. Dini, How does roughness kill adhesion? J. Mech. Phys. Solids 181 (2023) 105465.
[48] J. Luo, J. Liu, F. Zhang, X. Zhang, H. Shen, X. Wu, L. Wu, H. Xia, A novel calculation method for adhesive contact interactions of three-dimensional randomly rough surfaces, Acta Mech. Solida Sin. (2025).
[49] M. Paggi, J. Reinoso, A variational approach with embedded roughness for adhesive contact problems, Mech. Adv. Mater. Struct. 27 (20) (2018) 1731–1747.
[50] J. Bonari, M. Paggi, Viscoelastic effects during tangential contact analyzed by a novel finite element approach with embedded interface profiles, Lubricants 8 (12) (2020) 1–15.
[51] J. Bonari, M. Paggi, J. Reinoso, A framework for the analysis of fully coupled normal and tangential contact problems with complex interfaces, Finite Elem. Anal. Des. 196 (2021) 103605.
[52] J. Bonari, M. Paggi, D. Dini, A new finite element paradigm to solve contact problems with roughness, Int. J. Solids Struct. (2022) 111643.
[53] M.R. Marulli, J. Bonari, J. Reinoso, M. Paggi, A coupled approach to predict cone-cracks in spherical indentation tests with smooth or rough indenters, J. Mech. Phys. Solids 178 (2023) 105345.
[54] D. Haba, J. Kaufmann, A.J. Brunner, K. Resch, C. Teichert, Observation of elastic modulus inhomogeneities in thermosetting epoxies using AFM - Discerning facts and artifacts, Polymer 55 (16) (2014) 4032–4040.
[55] B.V. Derjaguin, V.M. Muller, Yu P. Toporov, Effect of contact deformations on the adhesion of particles, J. Colloid Interface Sci. 53 (2) (1975) 314–326.
[56] R.A. Sauer, P. Wriggers, Formulation and analysis of a three-dimensional finite element implementation for adhesive contact at the nanoscale, Comput. Methods Appl. Mech. Engrg. 198 (49–52) (2009) 3871–3883.
[57] Ning Yu, A.A. Polycarpou, Adhesive contact based on the Lennard-Jones potential: A correction to the value of the equilibrium distance as used in the potential, J. Colloid Interface Sci. 278 (2) (2004) 428–435.
[58] O.C. Zienkiewicz, R.L. Taylor, D. Fox, The Finite Element Method for Solid and Structural Mechanics, seventh ed., Elsevier Ltd, 2013.
[59] J.R. Barber, Contact mechanics, in: Solid Mechanics and Its Applications, vol. 250, Springer International Publishing, Berlin, 2018.
[60] S.D. Sjoerdsma, A.C.A.M. Bleijenberg, D. Heikens, The Poisson ratio of polymer blends, effects of adhesion and correlation with the Kerner packed grains model, Polymer 22 (5) (1981) 619–623.
[61] P.R. Guduru, C. Bull, Detachment of a rigid solid from an elastic wavy surface: Experiments, J. Mech. Phys. Solids 55 (2007) 473–488.
[62] P.R. Guduru, Detachment of a rigid solid from an elastic wavy surface: theory, J. Mech. Phys. Solids 55 (2007) 445–472.
[63] A. Carpinteri, G. Colombo, Numerical analysis of catastrophic softening behaviour (snap-back instability), Comput. Struct. 31 (4) (1989) 607–636.
[64] M. Ciavarella, Y. Xu, R.L. Jackson, The generalized Tabor parameter for adhesive rough contacts near complete contact, J. Mech. Phys. Solids 122 (2019) 126–140.
[65] K.L. Johnson, K. Kendall, A.D. Roberts, Surface energy and the contact of elastic solids, Proc. R. Soc. A 324 (1558) (1971) 301–313.
[66] V. Rey, J. Bleyer, Stability analysis of rough surfaces in adhesive normal contact, Comput. Mech. 62 (2018) 1155–1167, 8.